Title: Turbulent Droplet Breakage in a von Kármán Flow Cell

Authors: Krishnamurthy Ravichandar[a], R. Dennis Vigil [b], Rodney O. Fox[b], Stephanie Nachtigall[c],Andreas Daiss [c], Michal Vonka[c], Michael G. Olsen [a],

[a] Department of Mechanical Engineering, Iowa State University, Ames, IA, USA.

[b] Department of Chemical and Biological Engineering, Iowa State University, Ames, IA, USA

[c] BASF SE, Ludwigshafen am Rhein, Germany

Abstract:

Droplet dispersion in liquid-liquid systems is a crucial step in many unit operations throughout the chemical, food and pharmaceutic industries, where improper operation causes billions of dollar losses annually. A theoretical background for the description of droplet breakup has been established, but many assumptions are still unconfirmed by experimental observations. In this investigation, a von Kármán swirling flow device was used to produce homogeneous, low intensity turbulence suitable for carrying out droplet breakage experiments using optical image analysis. Individual droplets of known, adjustable, and repeatable sizes, were introduced into an isotropic turbulent flow field providing novel control over two of the most important factors impacting droplet breakage: turbulence dissipation rate and parent droplet size. Introducing droplets one at a time, large data sets were gathered using canola, safflower, and sesame oils for the droplet phase and water as the continuous phase. Automated image analysis was used to determine breakage time, breakage probability, and child droplet size distribution for various turbulence intensities. Breakage time and breakage probability were observed to increase with increasing parent droplet size, consistent with the classic and widely used Coulaloglou-Tavlarides breakage model (C-T model). The shape of the child drop size distribution function was found to depend upon the Weber number.

1. Introduction

Breakage of dispersed phase liquid droplets immersed in a second immiscible continuous liquid phase is a common phenomenon in the production of petrochemicals, polymers, metals, foods, and pharmaceuticals.[1,2] It is also vital for environmental management, such as cleaning up oil spills and cleaning leaking underground storage tanks. Moreover, droplet breakage - and the resultant evolution of the liquid-liquid interfacial area - has a substantial impact on interphase mass transfer and plays an important role in the performance of liquid-liquid reactors and liquid extraction process separation efficiency. Hence, a fundamental understanding of the role of the hydrodynamic phenomena that lead to droplet breakage is essential to predict and control interphase mass transport in these systems of interacting liquids.

Most models for droplet breakage in liquid-liquid turbulent flow are strongly influenced by theories of turbulent gas bubble and droplet breakup developed by Kolmogorov[3] and Hinze[4] and are based upon the assumption that breakage occurs due to collisions between droplets and turbulent eddies with sufficient energy to overcome cohesive forces that resist breakage. Consequently, these models are usually parameterized by the turbulent kinetic energy and turbulence dissipation rate, ε, and it is often assumed that only eddies equal to or smaller than the size of the droplet are effective for breakup. Implicit in this understanding is the assumption that breakage events result from a competition between disruptive inertial forces and the restorative surface force, and this competition is characterized by the Weber number, given by

$$\mathrm{We} = \frac{\tau_d d}{\sigma} = \frac{2\rho_c \varepsilon^{2/3} d^{5/3}}{\sigma}.$$

In the above expression d is the droplet diameter, τ_d is the droplet deformation stress, σ is the interfacial tension, and ρ_c is the continuous phase density.

Experimental validation of the traditional mechanistic understanding of droplet breakage described above has produced mixed results. [5–7] Whereas some studies confirm the assumption that breakage is induced by collisions of droplets with eddies smaller that the droplet diameter and often produce two child droplets (binary breakage), other investigations have demonstrated that droplets can be substantially stretched over a relatively long time scale (on the order of one second or more), thereby implying that it is the larger eddies with longer lifetimes that are most efficacious in producing breakage events. [4,8] This is especially true in cases where the droplet viscosity exceeds the continuous phase viscosity such that the viscosity ratio $\lambda = \mu_d/\mu_c > 1$ and where interfacial tension is less important. Some analyses also attempt to incorporate viscous, inertial, and interfacial forces by employing the "viscosity group", first introduced by Hinze and more commonly known as the Ohnesorge number, defined as

$$\mathrm{Oh} = \frac{\mu_d}{\sqrt{\sigma d \rho_d}}$$

where ρ_d is the droplet density.

The development and validation of mathematical models of breakage based upon mechanistic physical understanding of droplet behavior in turbulent flow is challenging not only because of the numerous variables that impact breakage events and the existence of multiple breakage regimes such as those described above, but also because of the difficulty in acquiring detailed and statistically significant experimental data sets for breakage events carried out under well-controlled conditions.[1,9,10] In particular, since droplet breakage strongly depends on the hydrodynamic environment, droplet breakage experiments should ideally be performed in a homogeneous flow field. Nevertheless, most existing experimental studies of turbulent drop breakage were performed using flow devices known to produce heterogeneous mixing environments, such as stirred tanks[11,12].

In this report, the authors describe attempts to overcome some important limitations of previous droplet breakage experiments by using high-speed photography to capture thousands of droplet breakage events in a von Kármán swirling flow device designed to (a) generate homogeneous isotropic turbulence in a region surrounding a droplet injection port, and (b) carefully control the size of parent droplets that are introduced one at a time into the breakage zone. Analysis of the acquired images provides statistical information concerning breakage rate, breakage probability, and child droplet size distribution. This information is compared with the predictions of some existing droplet breakage models to assess their accuracy and limitations.

2. Population Balance Equation Breakage Models

The application of droplet breakage models to predict the dynamic behavior of liquid-liquid emulsions in process equipment is usually achieved by formulating population balance equations (PBEs) and coupling them with fluid flow simulations. These statements of continuity can be expressed in terms of various internal variables. For spatially homogeneous systems and for spherical droplet morphology, a breakage PBE can be expressed in continuous form as

$$\frac{\partial c(v,t)}{\partial t} = -a(v)c(v,t) + \int_v^\infty a(u)b(v|u)c(u,t)du \qquad (1)$$

In the above expression $c(v,t)$ is the number concentration of droplets with volume v at time t. Hence, the first term on the right side of Eq. (1) represents the rate of breakage of droplets with volume v (normalized by the reactor volume), where $a(v)$ is the size-dependent rate coefficient having units of inverse time. In general, $a(v)$ also depends upon other factors, such as the turbulence dissipation rate, and it may also be interpreted in analogy to chemical rate constants consisting of the product of a frequency factor and reaction probability:

$$a(v) = \frac{P_b}{t_b} \qquad (2)$$

where P_b is the probability of breakage of a droplet of size v upon collision with an eddy, and t_b is the breakage time scale. The integral term on the right side of Eq. (1) represents the rate of production of droplets of volume v due to breakage of larger droplets, which depends not only on the rate of breakage of these larger droplets but also on the child distribution function $b(v|u)$, which is the conditional probability of generating a droplet of volume v from the breakage of a droplet of volume u.

Simulation of droplet size evolution in liquid-liquid emulsions requires a droplet breakage model capable of accurately predicting the breakage rate coefficient $a(v)$ and child distribution $b(v|u)$. Several theoretical and experimental investigations have been carried out to determine physical dependencies and mathematical forms for these breakage functions. One of the first and most widely used expressions for the droplet breakage rate coefficient was developed by Coulaloglou and Tavlarides (C-T) [13] to describe droplet breakage in stirred tanks:

$$a(v) = K_1 \varepsilon^{1/3} v^{-2/9} \exp\left[-\frac{K_2 \sigma}{\rho_d \varepsilon^{2/3} v^{5/9}}\right] \qquad (3)$$

or equivalently using diameter as the internal coordinate,

$$a'(d) = C_1 \varepsilon^{1/3} d^{-2/3} \exp\left[-\frac{C_2 \sigma}{\rho_d \varepsilon^{2/3} d^{5/3}}\right] = C_1 \varepsilon^{1/3} d^{-2/3} \exp\left[-\frac{C_2}{\mathrm{We}}\left(\frac{\rho_d}{\rho_c}\right)\right] \qquad (4)$$

The pre-factor in Eq. (4) represents a breakage frequency factor (not frequency itself) or equivalently the inverse of the droplet breakage time, t_b. The assumption that the kinetic energy distribution of droplets is the same as that of the eddies, and that only eddies smaller than a droplet are effective for its breakup, leads to the exponential term. This term can be interpreted as a probability function similar to the Arrhenius expression for chemical reactions, with the Weber number playing a role analogous to temperature and the constant C_2 representing a system-specific transition state barrier. In the several decades since the Coulaloglou-Tavlarides model (C-T model) was introduced, numerous modifications have been proposed including extensions to incorporate the effects of viscous forces.[13–15] However, the lack of experimental data for breakage time, breakage probability, and child distribution function in homogeneous hydrodynamic conditions has so far limited the ability to evaluate and discriminate between competing models.

3. Experimental Setup and Procedure

3.1 Experimental Setup

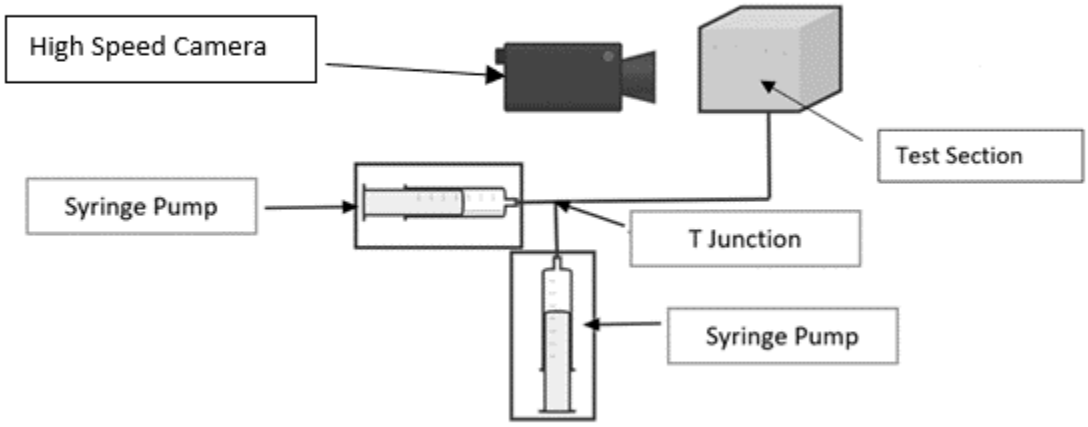

Figure 1. Schematic of the Experimental Setup

An experimental facility was constructed to investigate single droplet breakage at low turbulence intensities. The optically transparent experimental test section was designed and constructed such that it can generate a variable intensity turbulence field with a small mean velocity at the droplet injection location to ensure that the droplets remain in the field of view of the imaging system throughout the measurement time. To meet these objectives, the test section has been constructed similarly to a device used by De La Rosa Zambrano *et al*. [16] to study breakage of clusters of magnetic particles. The arrangement of the apparatus, including a droplet generator and image acquisition system is depicted in Fig. 1.

The test section consists of a polycarbonate tank with inner dimensions of 200.15 mm x 250.95 mm x 206.502 mm filled with deionized water as the continuous-phase fluid. The tank has a capacity of approximately 10.4 liters. Polycarbonate was used as it is a durable material with good resistance to impact and chemical attack. The transparency of the polycarbonate provides unimpeded optical access from all sides. The tank has a removable lid that allows access to the interior for cleaning between experiments. Compression gaskets (Durometer 30) and 160 1/4-inch Allen screws are used to create water-tight seals for lids at the top and bottom of the tank.

The left and right sides of the fluid test section are fitted with counter-rotating impellers of 200 mm diameter that generate a nearly homogeneous turbulent flow. Each impeller is connected to a motor and test section through the impeller drive shaft, which consists of two bearings rated for up to 10,000 rpm and a high-speed rotary shaft collar to prevent air or water leaks. The impellers are powered by DC motors with integrated drivers and controllers, rated for up to 3000 rpm. Varying the rotation speeds of the impellers varies the turbulence intensity inside the test section. The motors are supported by steel

motor mounts that isolate the fluid test section from vibrations. The motor and impeller shafts are connected with Oldham coupling discs to reduce vibration and noise.

Individual droplets fed to the fluid test section are generated as described in the next section. These droplets flow from the droplet generator through a 1/16-inch Teflon coated PTFE tube that enters the tank through the bottom wall using a 1/16 to 1/8-inch adapter connected to a stainless steel needle. Inside the tank, the droplets flow through the needle, which has inner and outer diameters of 0.41 and 0.74 mm, respectively. Images of droplets leaving the injection needle and subsequently undergoing breakage events are acquired using a Photonics high-speed digital camera fitted with a Sigma 50 mm macro lens capable of magnifications ranging between 1x-5x. The square field of view of the recorded images corresponds to side lengths of 117 mm. The f/32 aperture and focal length, and subject distance result in a depth of field of approximately 33 mm. The Photonics camera captures a sequence of 2048 images at speeds up to 2 kHz at full resolution. The high image capture speed enables the analysis of the entire breakup process of individual droplets.

3.3 Droplet Generation and Fluid Properties

Parent droplets are generated using two syringe pumps and a T-junction.[17] Cole Palmer syringe pumps control the flow rate of the fluids being dispensed. The IDEX P-633 T-junction has an inner diameter of 1.27 mm and a length of 9.40 mm. One syringe pump is used to control the flow of the continuous phase (water), which also serves as the carrier fluid in the droplet generator, whereas the second pump delivers the droplet phase (oil). The flow rates of the two phases control the size of the oil droplets pinched in the T-junction and that are subsequently injected into the test section. During the course of the experimental study, it was found that this droplet generation method was effective for generating droplets as small as 1 mm in diameter.

The three droplet test fluids chosen for this investigation were canola, safflower, and peanut oil. The visibility of each of these oils was increased using Dispersed Blue, a non-water-soluble dye. Because dye could affect interfacial tension and viscosity, these quantities were measured for the dyed oils. Viscosity was measured using a falling ball viscometer, and the liquid-liquid interfacial tension was measured using the pendant drop method for each of the oil-water combinations. The resulting values for viscosity and interfacial tension are shown in Table 1 for dyed oils and compared with values reported elsewhere in the literature.

Oil	**Interfacial Tension (N/m)**	**Literature Interfacial Tension** [18,19]	**Viscosity (mPa s)**	**Mean Literature Value Viscosity (mPa s)** [18,19]
Canola Oil	0.018	0.015-0.025	65.9	55
Safflower Oil	0.031	0.03-0.04	71.1	52.2
Sesame Oil	0.0115	0.005-0.014	43.3	35

Table 1. Measured oil-water interfacial tension and viscosity of droplet test fluids. Previously reported values from the literature are also listed.

3.4 Image Analysis

Figure 2. Example of a droplet frame before and after image processing.

A Matlab image analysis procedure was developed to extract breakage time, breakage probability, and child distribution information from the acquired images. In the first step, a background image (a frame that does not include any droplets) is subtracted from frames containing droplets. Subsequently, a binary mask and threshold is applied to further remove background noise. An example image showing the result of this procedure is shown in Fig. 2.

The last step in the procedure is to measure the droplet size pre- and post-breakage. This is achieved using the MATLAB function regionprops, which returns measurements for the set of properties for each 8-connected component (object) in the binary image. This function also stores the x- and y-coordinates of the centroids into a two-column matrix and determines the radius for each droplet. To investigate the

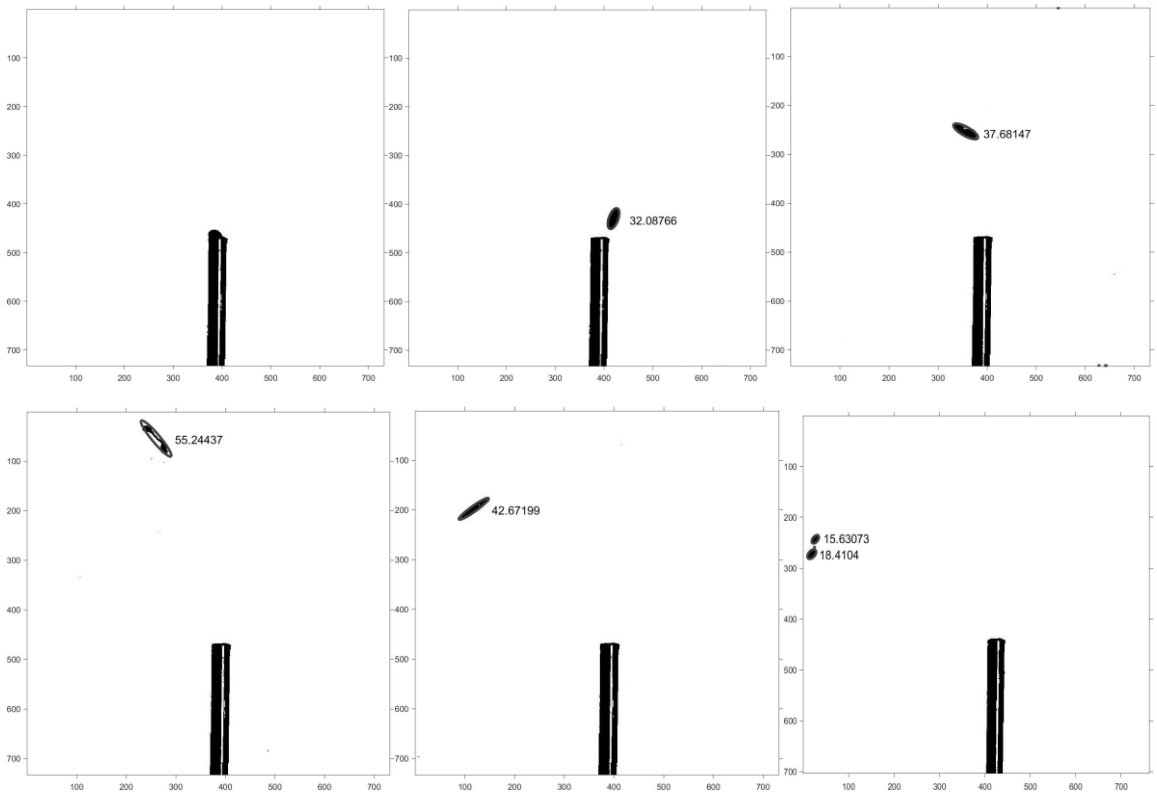

Figure 3. Canola oil droplet breakage sequence using image analysis software. The grey line seen in the figure shows fitted ellipsoids.

shape, the perimeter of the area is computed, as well as the minor and major axes of an ellipse with the same normalized second central moments as the area. An ellipsoid function was created which plots the ellipsoid shape with the specified droplet centers and radii, and this process is repeated for each frame, as shown in the examples in Fig. 3.

The accuracy of the fitting of ellipses to represent droplets, as described above, can be evaluated by considering whether the method conserves droplet mass. This can be achieved by comparing the sum of the volumes of child droplets with the volume of their parent droplet, which in turn requires some assumption about a third dimension for the droplets. Rather than assuming that all droplets are either oblate or prolate ellipsoids, in this work the lengths of the major and minor ellipse axes were averaged to estimate an equivalent sphere diameter from which the droplet volume was then computed. The droplet generation method allowed generation of droplets with diameter of 1.5 - 6 mm and allowed the size of droplet being injected into tank to be controlled. Based upon 1024 distinct droplet breakage events for canola oil, 1180 events for safflower, and 986 events for sesame oil, it was found that the computed sum of the volumes of child droplets range between 88%-95% of the parent droplet volumes. This degree of mass conservation was assumed as sufficient.

During the development of the image analysis methodology, definitions for breakage time and probability were also developed. Breakage time can have many definitions, but here it is defined as the interval between the droplet leaving the tip of the injection needle to the time a breakage event occurs in the observation volume. Breakage probabilities were computed from the experimental data by dividing the number of droplets undergoing breakage by the total number of droplets within a specific diameter size range (i.e., bin size). Droplet diameter bins were obtained using MATLAB's built-in histogram function which distributed the data into bins of 0.3 mm increments containing approximately 100 droplets each.

4. Results

4.1 Turbulence Dissipation Rate

As was discussed previously, the turbulence dissipation rate plays a crucial role in droplet breakage, and therefore an estimation of the value of this quantity is essential in order to validate droplet breakage models. Further, the fluid test cell was designed to minimize spatial heterogeneity and to produce homogeneous isotropic turbulence, and therefore it is necessary to demonstrate that the imaged volume (the breakage zone) in the von Kármán reactor is indeed relatively homogeneous.

Experimental measurement of ε is difficult even when using sophisticated methods such as stereoscopic particle image velocimetry, from which at most 7 of 9 components of the deformation stress tensor can be deduced. Consequently, 3-dimensional simulations were performed for the fluid test section using the computational fluid dynamics software Ansys FLUENT 2021 with the k-ε and Reynolds stress turbulence models. Grid convergence studies were performed, resulting in a final structured linear mesh of 817,170 nodes and more than 2.2 million elements. Figure 3b depicts the Ansys FLUENT simulation domain for the von Kármán box, which includes the counter-rotating disc impellers with vanes and 6 walls.

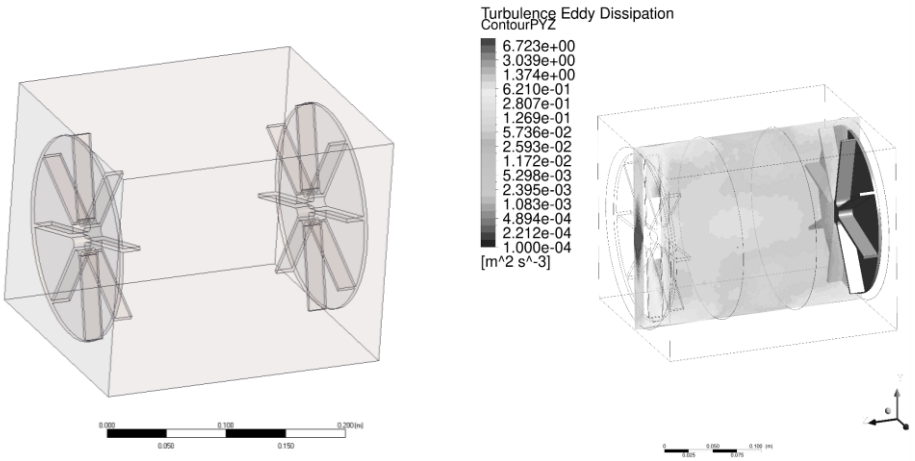

(a) (b)

Figure 4. (a) Ansys model of the tank geometry and (b) contour plot of the average turbulence dissipation rate near the droplet injection tube as calculated in the simulations for an impeller speed of 65 rpm.

The k-ε turbulence model was chosen because it is known to provide superior performance for flows involving rotation as well as boundary layers under strong adverse pressure gradients, separation and recirculation.[20–22] Figure 4b shows a typical contour plot of the computed turbulence dissipation rate in a vertical plane orthogonal to the impellers and passing through the impeller axes of rotation. As one would expect, the turbulence dissipation rate is greatest at the impeller tips and progressively decreases moving towards the center of the tank at the point of droplet injection, which is located at approximately the center of the device. It is evident in Fig. 4b that there is little variation in ε with position near the center of the box. Nevertheless, a mean dissipation rate was calculated by using the mean value for the imaged area in a vertical plane passing through the needle tip and the rotation axes of the impellers. The resulting computed mean turbulence dissipation rates were found to be 0.08251 m^2s^{-3} and 0.1065 m^2s^{-3} for impeller speeds of 65 and 85 rpm, respectively.

4.2 Breakage Time

Breakage time can have many definitions, but here it is defined as the interval between the droplet leaving the tip of the injection needle to the time a breakage event occurs in the observation volume. Breakage time models developed by Lasheras *et al*.,[23] Coulaloglou and Tavlarides (C-T) ,[13] and Raikar *et al*. [24] predict that breakage time increases with increasing parent droplet diameter. This prediction was validated in experiments on oil breakup in a stirred tank by Solsvik and Jakobsen. [25]

Mean breakage time as a function of the parent droplet size in the current study is presented in Fig. 5. Parent droplets were binned in 0.3 mm increments such that each bin contained at least 100 unique droplets that underwent breakage. Breakage times within a bin were found to be approximately normally distributed. Hence, error bars shown in Fig. 5 represent standard errors.

Figure 5 demonstrates that, consistent with previous experiments, droplet breakage time increases monotonically with increasing parent drop diameter at fixed impeller speed. Comparing Figs. 5a and 5b, it is also apparent that increasing impeller speed (and therefore ε) from 65 rpm to 85 rpm decreases breakage time. At higher impeller speeds turbulent eddies carry more kinetic energy, thereby increasing the deformation stress exerted on droplets.

Breakage time predictions from the Coulaloglou and Tavlarides (C-T) model (the inverse of the prefactor in Eq. 4) were fit to breakage time data as shown in Fig. 5. As previously stated, the C-T model requires both the turbulence dissipation rate and the parent droplet diameter to calculate breakage time. Using the experimental parameters for the various cases, the coefficient C_1 in the model was found to be 0.01112 for canola oil, 0.007296 for safflower oil, and 0.02661 for sesame oil, all of which are comparable to the value of $C_1 = 0.0462$ obtained by Coulaloglou and Tavlarides (C-T) in a series of experiments in a stirred tank using water-kerosene-dichlorobenzene droplets.[1,10]

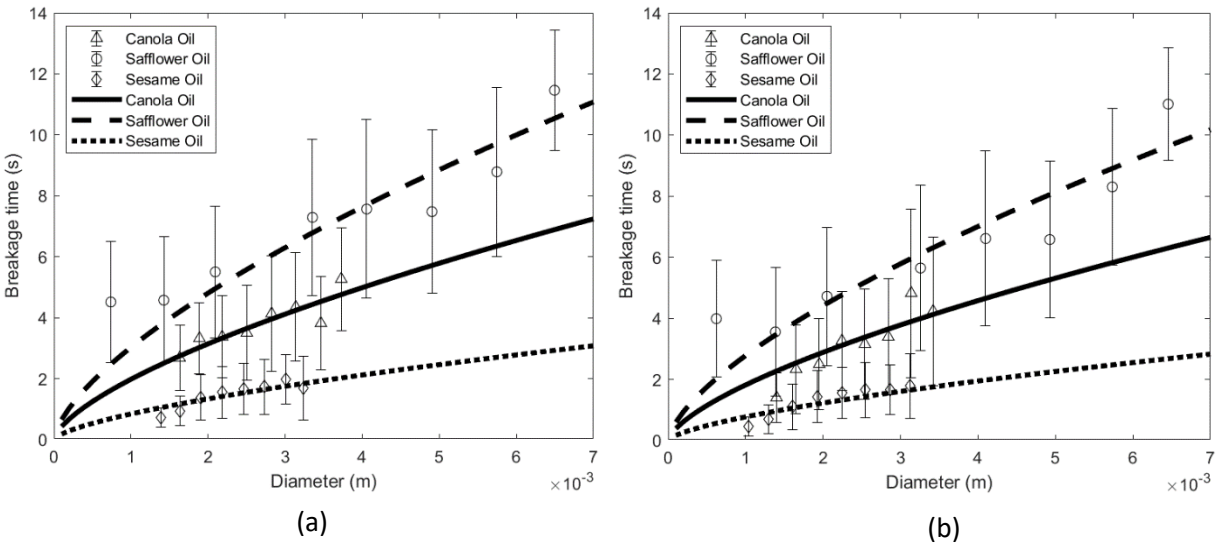

Figure 5. (a) Breakage time versus parent droplet diameter at 65 rpm with symbols representing experimental data and lines representing C-T model predictions, and (b) breakage time versus parent droplet diameter at 85 rpm.

4.3 Stabilization Stress and Deformation Stresses

If droplet breakage is understood to occur as a result of competition between stresses that cause and resist droplet deformation, it follows that when these competing stresses are equal, the droplets have an equal chance of either breaking or retaining their integrity. If external viscous stresses can be neglected, then the deformation stress, τ_{def}, is caused by turbulent pressure fluctuations and it can be calculated by

assuming that turbulent structures in the inertial subrange are responsible for the droplet breakup, resulting in the following expression.[2]

$$\tau_{def} = 2\rho_c(\varepsilon d)^{\frac{2}{3}} \tag{5}$$

The droplet is stabilized by the interfacial tension. The viscous and capillary stabilizing stresses can be expressed as:[4]

$$\tau_{\mu} = \frac{\mu_d}{d_p}\sqrt{\frac{\tau_{def}}{\rho_d}} \tag{6}$$

$$\tau_{\sigma} = \frac{\sigma}{d_p} \tag{7}$$

where μ_d is the viscosity of the dispersed phase, d_p is the parent diameter, σ is the interfacial tension, and ε is turbulence dissipation rate. Plotting the deformation stress described by Eq. (5) and the stabilization stress, defined as the sum of Eqs. (6) and (7) leads to Fig. 6. In view of the above discussion, it can be expected that the intersections of these curves may be predictive of characteristic droplet diameters having an equal probability of either breaking up or retaining their integrity while undergoing a deformation event. During the calculation of interfacial and viscous stabilization stress it was found that

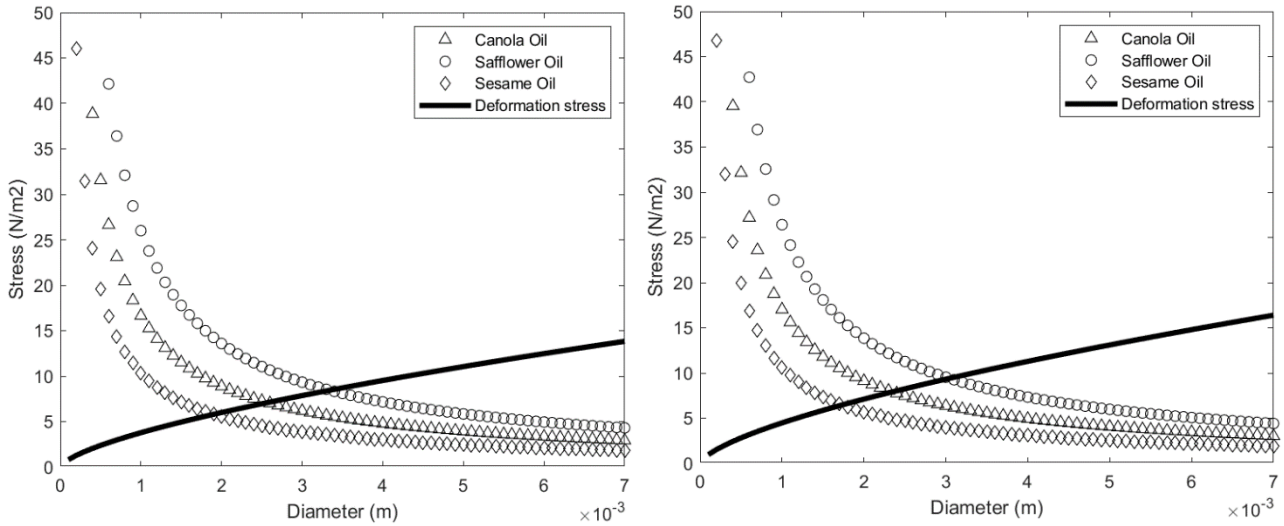

Figure 6. Stresses as a function of droplet diameter. Symbols represents stabilization stress whereas the line represents deformation stress for (a) 65 rpm and (b) 85 rpm.

the interfacial stabilization stress accounted for approximately 70% of total stabilization stress while the viscous stabilization stress only contributed 30%. This lower dependency on viscous stabilization stress allowed for the usage of C-T model as its breakage probability does not have an exponential component which relates to the viscosity.

For parent droplet diameters of 2 – 4 mm for sesame oil, the deformation stresses at 65 rpm and 85 rpm are significantly greater than what is needed to overcome the stabilization stress, and thus the droplet almost always undergoes breakage. This can be accounted for by the higher Weber number for sesame oil droplets compared to the other oils. For example, for sesame oil, We = 2.2 for 3 mm diameter parent droplets, compared to Weber numbers of only 0.8 for safflower oil and 1.34 for canola oil droplets of the same diameter.

4.4 Breakage Probability

Breakage probabilities were computed from the experimental data by dividing the number of droplets undergoing breakage by the total number of droplets within a specific diameter size range (bin size). Droplet diameter bins were obtained using MATLAB's built-in histogram function which distributed the data into bins of 0.3 mm increments containing approximately 100 droplets each.

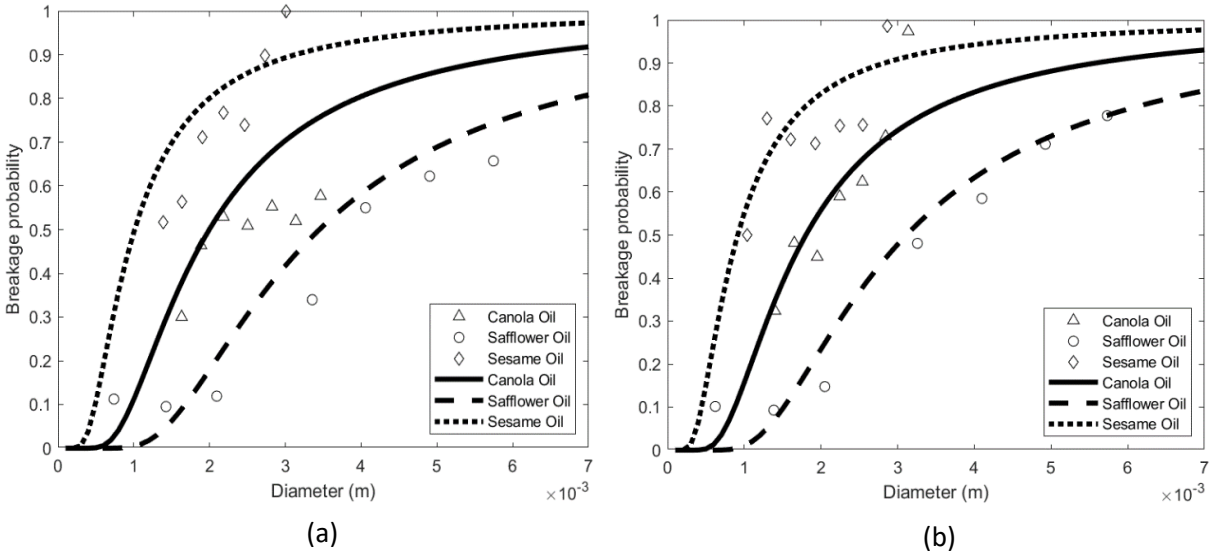

Figure 7. (a) Breakage probability vs. parent droplet diameter for 65 rpm with symbols representing experimental data and lines representing C-T model predictions, and (b) breakage probability vs. parent droplet diameter for 85 rpm.

Figure 7 shows droplet breakage probabilities for the three test fluids at impeller speeds of 65 rpm and 85 rpm. It can be observed in Fig. 7 that the droplet breakage probability increases with increasing droplet diameter for fixed turbulence dissipation rate. Galinat *et al*. [26,27] and Ashar *et al*.[28] found in their experimental investigations that a critical Weber number exists below which breakage is unlikely. This critical Weber is dependent on the parent droplet diameter and flow parameters such as turbulence dissipation rate and flow velocity. In this study, we identify a critical Weber number computed from critical droplet diameters with 50% probability of undergoing breakup. In principle, these critical droplet diameters can be found from the intersections of the deformation and stabilizing stresses depicted in

Fig. 6, and this hypothesis appears to be verified by comparing those predictions with experimentally measured critical droplet diameters, as shown in Table 2.

Table 2 shows close agreement between measured critical diameters and those predicted from the intersection of the stresses shown in Fig. 6. At the lowest rpm considered (65 rpm), safflower oil has a minimum parent droplet diameter of 3 mm, which is significantly higher than the 1.5 mm critical diameter for sesame oil. This difference is due to the fact that the oil-water interfacial tension is nearly three times greater for safflower oil (31mN/m) than for sesame oil (11.5 mN/m).

RPM	Canola oil (measured) (mm)	Canola Oil (predicted) (mm)	Safflower Oil (measured) (mm)	Safflower Oil (predicted) (mm)	Sesame Oil (measured) (mm)	Sesame Oil (predicted) (mm)
65	2.2	2.3	3.6	3.5	1.5	1.75
85	2.0	2.1	3.1	3.0	1.3	1.6

Table 2. Comparison of critical droplet diameters (mm) determined from experiments and from the intersections of the deformation and stabilization stress curves in Fig. 6.

The experimentally measured breakage probabilities can also be compared with the C-T model predictions after fitting the model parameter C_2.[7] This parameter was found to have values 0.2116 for canola oil, 0.3142 for safflower oil, and 0.811 for sesame oil. Previous studies by other investigators report values of C_2 ranging from 0.106- 0.39 for various fluids. [10,13] The C_2 values for sesame oil exceed the range of values reported in these other studies, and this is due to fact that the interfacial tension and viscosity for sesame oil are significantly lower than for the fluids in those investigations, thereby resulting in a larger Weber number than in the previous studies.

In Fig. 7, C-T model predictions are plotted as lines, and the experimental data for each of the test fluids are plotted as scatter points. The results shown in Fig. 7 suggest that while the C-T model does produce predictions that provide reasonable agreement with the experimental measurements at both 65 rpm and 85 rpm, the fit with the experimental data is better for the higher impeller speed of 85 rpm.

4.5 Breakage Rate Coefficient

The breakage rate coefficient a' in Eq. (4) can be computed from the experimental data by dividing the breakage probability by breakage time. Figure 8 compares these experimentally measured values for a' with C-T model predictions[13] using the parameters C_1 and C_2 obtained in the previous two sections. The results shown in Fig. 8 suggest that the C-T model predictions are reasonably accurate over the range of parent droplet sizes considered.

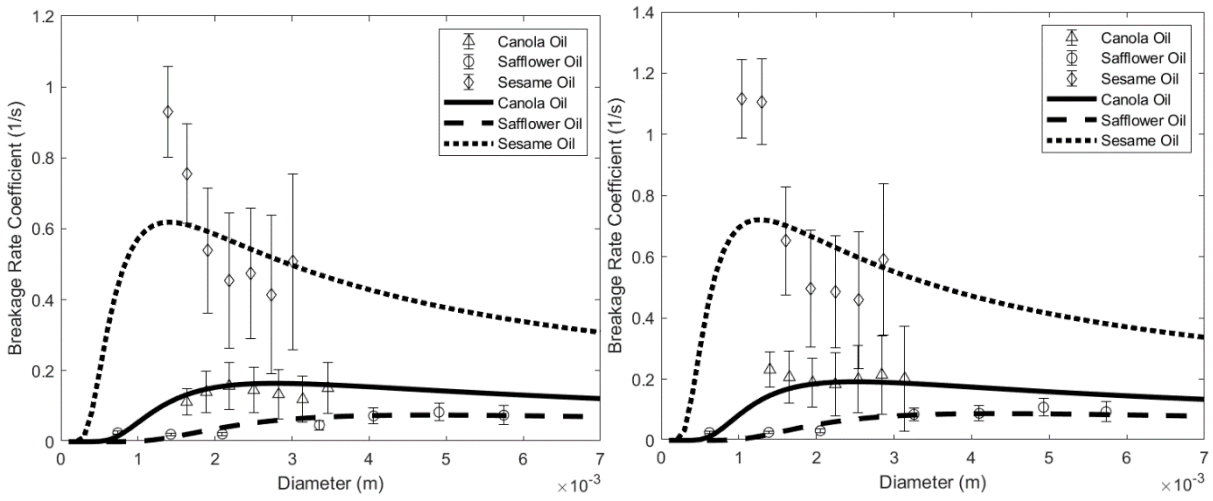

Figure 8. (a) Breakage rate coefficient vs. parent droplet diameter for 65 rpm. Symbols represent experimental data and lines represent C-T model predictions. (b) Breakage rate coefficient vs. parent droplet diameter at 85 rpm.

Figure 8 also appears to show that the C-T model provides better predictions for canola and safflower oil than for sesame oil. As was mentioned in the discussion of breakage probability, the greater disparity observed between experimental values and model predictions for the sesame oil breakage coefficient may be due to the longer breakage times for sesame oil, which in turn could lead to droplets leaving the imaged volume before undergoing breakage. In such a circumstance, the experimentally observed breakage probability could be misleading because of undercounting of breakage events.

4.6 Child Size Distribution

As with the breakage rate coefficient a', the functional form of the child droplet distribution $b'(d|D)$, which describes the conditional probability that a droplet with diameter d is produced by the breakage of a droplet of diameter $D > d$, may depend upon parameters relevant to a specific breakage regime. Physical and mathematical constraints on the functional form of the child distribution can be deduced by considering the volume-based internal coordinate formulation (assumes constant drop density), i.e., $b(v|u)$ as in Eq. (1).[29] Specifically, continuity requires that $b(v|u)$ be normalized such that

$$\int_0^u v b(v|u) dv \; = \; u \tag{8}$$

Further, the expected number of droplets from a single breakage event is given by

$$\overline{N} = \int_0^u b(v|u) dv. \tag{9}$$

It should also be recognized that in the case of binary breakup ($\overline{N} = 2$), the child distribution function must be symmetric such that $b(v|u) \; = \; b(u - v|u)$. However, for any value $\overline{N} > 2$ (non-binary breakup), $b(v|u)$ cannot be symmetric, and additional continuity requirements for the case of multiple breakage imply that $b(v|u)$ must be a monotonically decreasing function of the child droplet size v. [29]

For the fluids studied in this investigation, only binary breakage events were observed, and therefore symmetric child distribution functions should be produced. In some experiments, the initial breakage event was closely followed by secondary binary breakage of a child droplet, but these secondary breakage events were not included in the child distribution statistics. As was discussed in Section 3.4, the ellipsoid volume calculation procedure in the image analysis software is prone to small but meaningful errors in droplet volume. These errors, if uncorrected, will lead to asymmetric child distributions. For this reason, child distributions were constructed by using the difference between parent and largest child droplet volumes obtained from the image analysis software in order to compute the volume of the smaller child so that volume is conserved. The largest parent droplet was chosen from the image analysis as it allowed for more accurate measurement of the droplet volume and is not affected by the thresholding as would be case with the smaller droplet.

In the previous discussions of breakage probability and breakage time, the C-T model predictions were compared with experimental data, as the underlying model assumptions for those quantities are largely satisfied for the fluid pairs and flow conditions studied. However, for child size distributions, the C-T model assumes binary breakage with a normal child size distribution irrespective of the magnitudes of the disruptive and cohesive stresses. Such an assumption is known to be faulty, particularly in cases for which the deformation stress significantly exceeds the stabilizing stress (as is the case for the experiments reported here using sesame oil). In such instances, the child distribution function exhibits bimodal behavior. [1,10] For this reason, predictions of the C-T model are not shown in Figs. 9-14.

Figures 9 and 10 show canola oil child droplet diameter (plotted as fractions of the parent droplet volume) distributions for various parent droplet diameters for 65 rpm and 85 rpm. In all cases, at least 100 droplet breakage events were observed. The distributions appear to be monomodal, with strong bias towards equal sized child droplets for smaller sized parent droplets. As can be seen in Figs. 9 and 10, as the diameter of the parent droplet for canola oil increases, the probability distribution slowly begins to transition from a monomodal distribution to a bimodal distribution. This can be attributed to the deformation stress significantly exceeding the stabilization stress at the largest diameters, as both these stresses are dependent on the parent diameter size. It is also important to observe that for a similar parent droplet diameter, increasing the turbulence dissipation rate (i.e., increasing the impeller rotation speed) results in an increased width of the distribution of child droplet diameters.

Figures 11 and 12 show safflower oil child droplet diameter (plotted as fractions of the parent droplet volume) distributions for various parent droplet diameters for 65 rpm and 85 rpm. In all cases, at least 100 droplet breakage events were observed. The overall trend that can be seen in Figs. 11 and 12 is that distributions appear to be monomodal, with strong bias towards equal sized child droplets. However, it is important to observe that Figs. 11a and 12a show bimodal behavior, and this can be accounted for by these parent droplet diameters being below the critical diameter of 3.6 mm and 3.1 mm for 65 rpm and 85 rpm, respectively, meaning that probability of breakage is lower than 50%. At parent diameter below the critical diameter, the stabilization stresses are greater than deformation stresses. As such, the breakage, although a rare event, must occur due to factors other than the competition between stabilization and deformation stresses (such as perhaps the droplet emerging from the injection needle already deformed, or stretching of the droplet due to droplet motion), and these other factors result in bimodal breakup. Similarly to canola oil, for safflower oil droplets increasing the turbulence dissipation resulted in an increased width of the distribution of child droplet diameters.

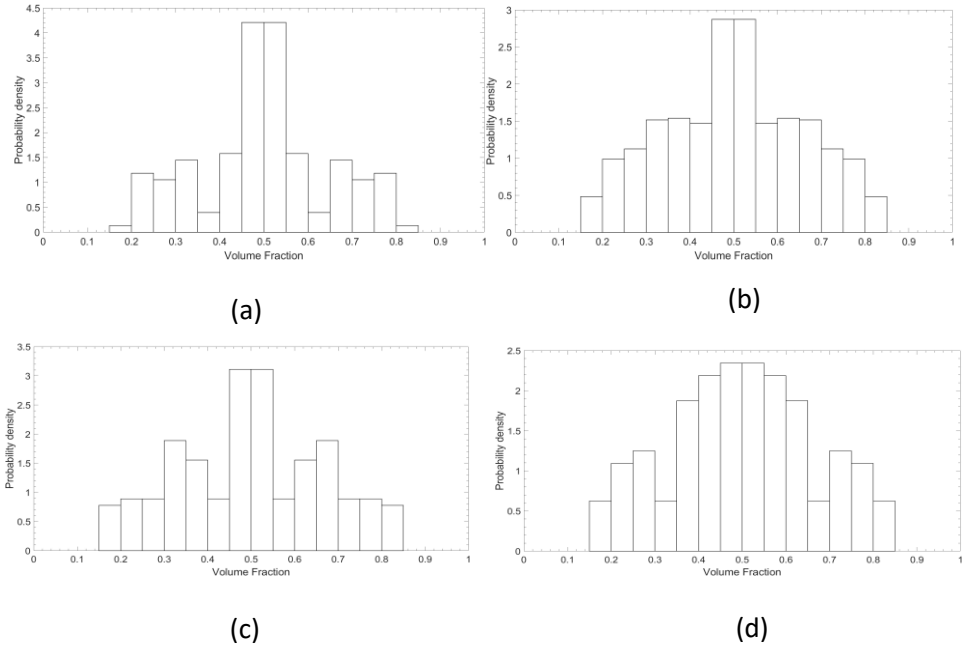

Figure 9. Canola oil daughter droplet size distribution for 65 rpm for parent droplet diameters of (a) 1.6 mm, (b) 1.9 mm, (c) 2.2 mm, (d) 2.5 mm.

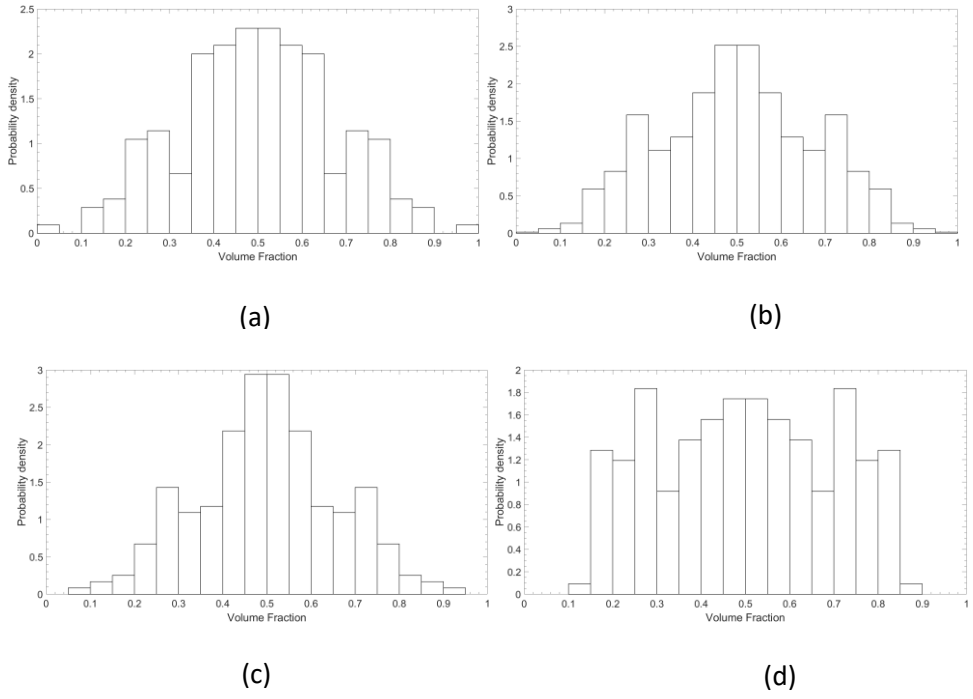

Figure 10. Canola oil daughter droplet size distribution for 85 rpm for parent droplet diameters of (a) 1.5 mm, (b) 1.8 mm, (c) 2.1 mm, (d) 2.4 mm.

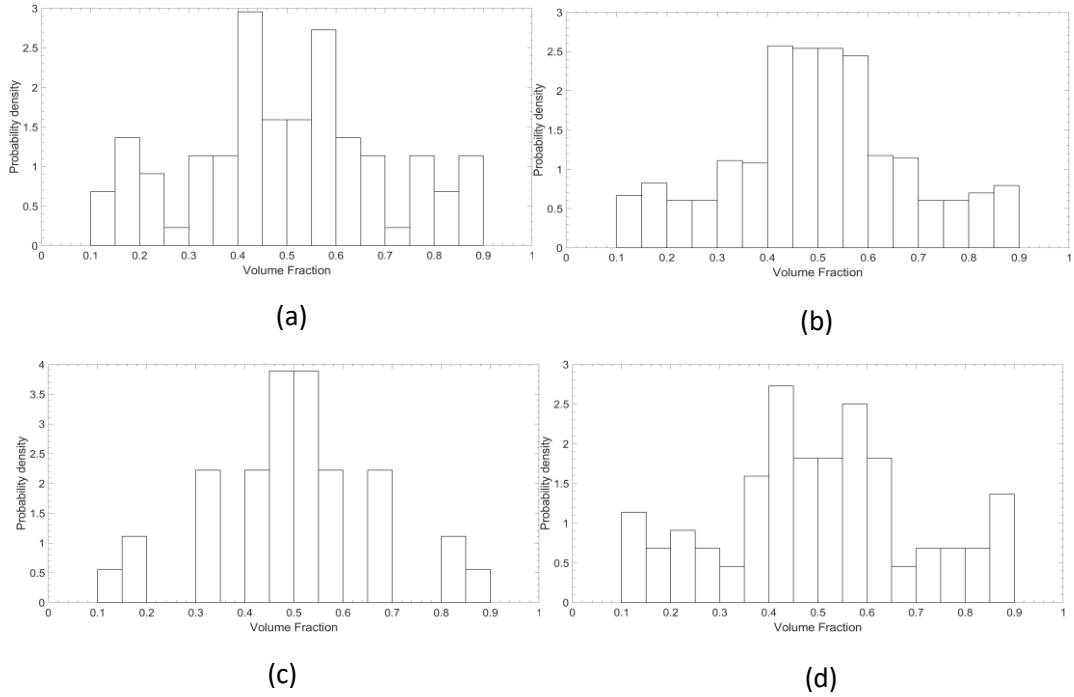

Figure 11. Safflower oil daughter droplet size distribution for 65 rpm for parent droplet diameters of (a) 1.8 mm, (b) 2.7 mm, (c) 3.6 mm, (d) 4.5 mm.

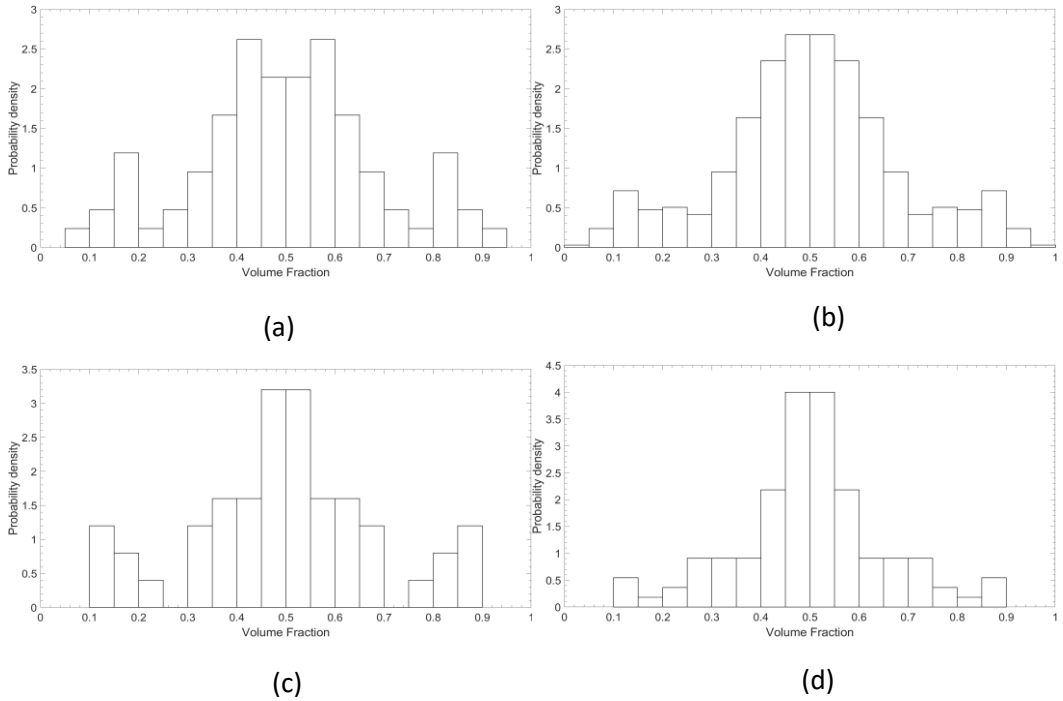

Figure 12. Safflower oil daughter droplet size distribution for 85 rpm for parent droplet diameters of (a) 1.8 mm, (b) 2.7 mm, (c)3.6 mm, (d) 4.5 mm.

In contrast to canola oil and safflower oil, the child droplet diameter distribution function for sesame oil is not monomodal, and therefore describes breakage events that favor production of two droplets with widely disparate sizes, as shown in Figs. 13 and 14. The multimodal distribution functions shown in Figs. 13 and 14 are characteristic of child distributions described as either "M" shaped or "U" shaped, which have been observed to arise when the deformation stress exceeds the stabilization stress, thus leading to greater stretching of droplets undergoing breakage. It can be seen from Figs. 13 and 14 that as the size of the parent droplet increases, the M/U shaped distribution becomes more prominent as the deformation stress increases with droplet diameter size while stabilization stress decreases respectively. Increasing the deformation stress through increasing the turbulence dissipation rate also causes a similar effect.

Sesame oil has both low interfacial tension and viscosity compared to canola oil and safflower oil. Hence, the interfacial and internal viscous stresses, both of which stabilize droplets, are not as large as for the other oils, and therefore the deformation stress required to cause droplet breakage is lower, as is shown in Fig. 6. Droplet breakup image sequences for sesame oil show that these droplets undergo much larger deformation compared to canola and safflower oil before breakage occurs, which in turn produces disparate child droplets. Indeed, for the sesame oil experiments carried out here, the deformation stress significantly exceeds the stabilization stresses. If the turbulence dissipation rate were to be lowered such that the deformation and stabilization stresses were more equal, it is likely that a monomodal distribution would have been observed as in the cases for canola and safflower oil.

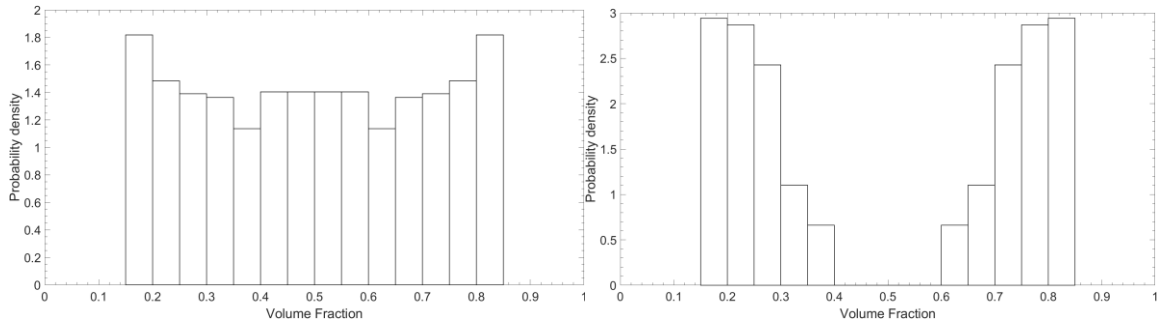

(a) (b)

Figure 13. Sesame oil daughter droplet size distribution for 65 rpm for parent droplet diameters of (a) 2.04 mm, (b) 2.32 mm

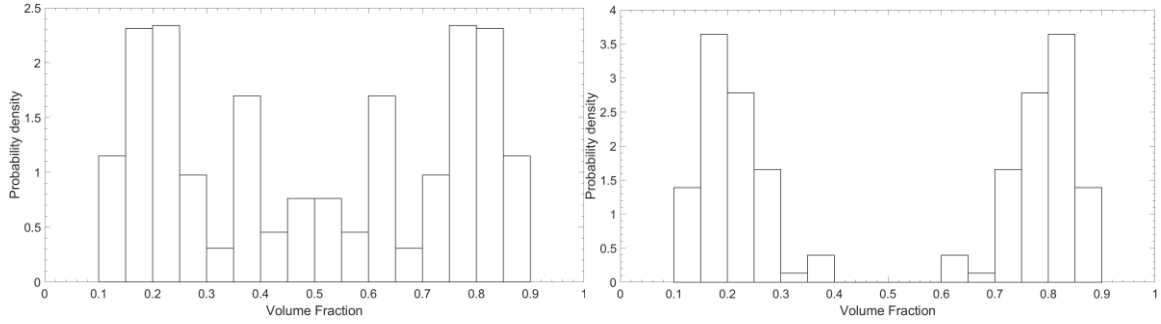

(a) (b)

Figure 14. Sesame oil daughter droplet size distribution for 85 rpm for parent droplet diameters of (a) 2.04 mm, (b) 2.32 mm

5. Summary and Conclusions

A method for performing optically-based droplet breakage experiments in a homogenous turbulent flow using a von Kármán swirling flow device was developed. The apparatus was used to collect breakage data, including breakage time, probability, and child size distributions for various vegetable oil droplets undergoing breakage in water. In addition, a droplet generation protocol was developed that provided a means for reproducibly introducing specific parent droplet sizes into the von Kármán flow cell. These two innovations allow for experimental control of two of the most important factors that impact droplet breakage, namely turbulence dissipation rate and droplet size. By introducing droplets one at a time into the fluid flow test section and by using high-speed photography and automated image analysis, it was demonstrated that a large number of droplet breakage events could be collected and used to evaluate a droplet breakage model.

For the fluid pairs tested, the Ohnesorge number was small, thereby suggesting that viscous resistance to drop deformation was less important when compared to the disruptive inertial stresses and cohesive interfacial stress. Such conditions satisfy some important assumptions of the classic Coulaloglou-Tavlarides droplet breakage model, and therefore, the experimental results for breakage time and breakage probability were used to compute a breakage rate coefficient, which in turn was compared to C-T model predictions. For the fluids tested, these model predictions compared well with the experimental results.

Both the breakage probability and the breakage time were found to increase with an increase in parent droplet size, consistent with CT model predictions, particularly for the fluids with high interfacial tension and viscosity (canola oil and safflower oil), which exhibit binary breakage.

The canola oil and safflower oil child droplet distributions appear to be monomodal, with strong bias towards equal sized child droplets for smaller sized parent droplets. As the diameter of the parent droplet for canola oil increases, the probability distribution slowly begins transitioning from a monomodal distribution to a bimodal distribution. This can be attributed to the deformation stress significantly exceeding the stabilization stress as both these stresses are dependent on the parent diameter size. For similar parent droplet diameters, increasing the turbulence dissipation rate results in broadening of the distribution of child droplet diameters. In contrast, for experiments carried out using sesame oil, which has both low viscosity and low interfacial tension, droplets were observed to undergo greater deformation and the breakage events produced bimodal breakage distribution functions.

6. Acknowledgements

The authors would like to thank Annika Lehan for assistance in carrying out droplet breakage experiments and Dr. Manjil Ray and Saad Aftab, all from Iowa State University, for helpful discussions.

References

(1) Herø, E. H.; la Forgia, N.; Solsvik, J.; Jakobsen, H. A. Single Drop Breakage in Turbulent Flow: Statistical Data Analysis. *Chemical Engineering Science: X* **2020**, *8*. https://doi.org/10.1016/j.cesx.2020.100082.

(2) Nachtigall, S.; Zedel, D.; Kraume, M. Analysis of Drop Deformation Dynamics in Turbulent Flow. *Chinese Journal of Chemical Engineering* **2016**, *24* (2), 264–277. https://doi.org/10.1016/j.cjche.2015.06.003.

(3) Kolmogorov, A. N. Dissipation of Energy in the Locally Isotropic Turbulence (English Translation by V. Levin, 1991). *Proceedings of the Royal Society A: Mathematical, Physical and Engineering Sciences* **1941**, *434* (1890).

(4) Hinze, J. O. Fundamentals of the Hydrodynamic Mechanism of Splitting in Dispersion Processes. *AIChE Journal* **1955**, *1* (3). https://doi.org/10.1002/aic.690010303.

(5) Risso, F.; Fabre, J. Oscillations and Breakup of a Bubble Immersed in a Turbulent Field. *Journal of Fluid Mechanics* **1998**, *372*. https://doi.org/10.1017/S0022112098002705.

(6) Luo, H.; Svendsen, H. F. Theoretical Model for Drop and Bubble Breakup in Turbulent Dispersions. *AIChE Journal* **1996**, *42* (5). https://doi.org/10.1002/aic.690420505.

(7) Sleicher, C. A. Maximum Stable Drop Size in Turbulent Flow. *AIChE Journal* **1962**, *8* (4). https://doi.org/10.1002/aic.690080410.

(8) Collins, S. B.; Knudsen, J. G. Drop-size Distributions Produced by Turbulen Pipe Flow of Immiscible Liquids. *AIChE Journal* **1970**, *16* (6). https://doi.org/10.1002/aic.690160634.

(9) Karimi, M.; Andersson, R. Dual Mechanism Model for Fluid Particle Breakup in the Entire Turbulent Spectrum. *AIChE Journal* **2019**, *65* (8). https://doi.org/10.1002/aic.16600.

(10) Maaß, S.; Kraume, M. Determination of Breakage Rates Using Single Drop Experiments. *Chemical Engineering Science* **2012**, *70*, 146–164. https://doi.org/10.1016/j.ces.2011.08.027.

(11) Zaccone, A.; Gäbler, A.; Maaß, S.; Marchisio, D.; Kraume, M. Drop Breakage in Liquid-Liquid Stirred Dispersions: Modelling of Single Drop Breakage. *Chemical Engineering Science* **2007**, *62* (22). https://doi.org/10.1016/j.ces.2007.07.026.

(12) Chatzi, E. G.; Gavrielides, A. D.; Kiparissides, C. *Generalized Model for Prediction of the Steady-State Drop Size Distributions in Batch Stirred Vessels*; UTC, 1989; Vol. 28.

(13) Coulaloglou, C. A.; Tavlarides, L. L. Description of Interaction Processes in Agitated Liquid-Liquid Dispersions. *Chemical Engineering Science* **1977**, *32* (11), 1289–1297. https://doi.org/10.1016/0009-2509(77)85023-9.

(14) Zhong, C.; Komrakova, A. Liquid Drop Breakup in Homogeneous Isotropic Turbulence. *International Journal of Numerical Methods for Heat and Fluid Flow* **2019**, *29* (7), 2407–2433. https://doi.org/10.1108/HFF-09-2018-0490.

(15) Martínez-Bazán, C.; Montañés, J. L.; Lasheras, J. C. On the Breakup of an Air Bubble Injected into a Fully Developed Turbulent Flow. Part 2. Size PDF of the Resulting Daughter Bubbles. *Journal of Fluid Mechanics* **1999**, *401*, 183–207. https://doi.org/10.1017/S0022112099006692.

(16) de La Rosa Zambrano, H. M.; Verhille, G.; le Gal, P. Fragmentation of Magnetic Particle Aggregates in Turbulence. *Physical Review Fluids* **2018**, *3* (8). https://doi.org/10.1103/PhysRevFluids.3.084605.

(17) Liu, H.; Zhang, Y. Droplet Formation in a T-Shaped Microfluidic Junction. *Journal of Applied Physics* **2009**, *106* (3). https://doi.org/10.1063/1.3187831.

(18) FISHER, L. R.; MITCHELL, E. E.; PARKER, N. S. Interfacial Tensions of Commercial Vegetable Oils with Water. *Journal of Food Science* **1985**, *50* (4). https://doi.org/10.1111/j.1365-2621.1985.tb13052.x.

(19) Cong, Y.; Zhang, W.; Liu, C.; Huang, F. Composition and Oil-Water Interfacial Tension Studies in Different Vegetable Oils. *Food Biophysics* **2020**, *15* (2). https://doi.org/10.1007/s11483-019-09617-8.

(20) Argyropoulos, C. D.; Markatos, N. C. Recent Advances on the Numerical Modelling of Turbulent Flows. *Applied Mathematical Modelling*. 2015. https://doi.org/10.1016/j.apm.2014.07.001.

(21) Liu, Y.; Olsen, M. G.; Fox, R. O. Turbulence in a Microscale Planar Confined Impinging-Jets Reactor. *Lab on a Chip* **2009**, *9* (8). https://doi.org/10.1039/b818617k.

(22) Meslem, A.; Bode, F.; Croitoru, C.; Nastase, I. Comparison of Turbulence Models in Simulating Jet Flow from a Cross-Shaped Orifice. *European Journal of Mechanics, B/Fluids* **2014**, *44*. https://doi.org/10.1016/j.euromechflu.2013.11.006.

(23) Eastwood, C. D.; Armi, L.; Lasheras, J. C. The Breakup of Immiscible Fluids in Turbulent Flows. *Journal of Fluid Mechanics* **2004**, *502*. https://doi.org/10.1017/S0022112003007730.

(24) Raikar, N. B.; Bhatia, S. R.; Malone, M. F.; Henson, M. A. Experimental Studies and Population Balance Equation Models for Breakage Prediction of Emulsion Drop Size Distributions. *Chemical Engineering Science* **2009**, *64* (10). https://doi.org/10.1016/j.ces.2009.01.062.

(25) Solsvik, J.; Jakobsen, H. A. Development of Fluid Particle Breakup and Coalescence Closure Models for the Complete Energy Spectrum of Isotropic Turbulence. *Industrial and Engineering Chemistry Research* **2016**, *55* (5), 1449–1460. https://doi.org/10.1021/acs.iecr.5b04077.

(26) Galinat, S.; Masbernat, O.; Guiraud, P.; Dalmazzone, C.; Noïk, C. Drop Break-up in Turbulent Pipe Flow Downstream of a Restriction. *Chemical Engineering Science* **2005**, *60* (23). https://doi.org/10.1016/j.ces.2005.05.012.

(27) Galinat, S.; Torres, L. G.; Masbernat, O.; Guiraud, P.; Risso, F.; Dalmazzone, C.; Noik, C. Breakup of a Drop in a Liquid-Liquid Pipe Flow through an Orifice. *AIChE Journal* **2007**, *53* (1). https://doi.org/10.1002/aic.11055.

(28) Single Droplet Breakup in a Rotor-Stator Mixer _ Elsevier Enhanced Reader.

(29) McGrady, E. D.; Ziff, R. M. Shattering Transition in Fragmentation. *Physical Review Letters* **1987**, *58* (9). https://doi.org/10.1103/PhysRevLett.58.892.